



Isolated Manganese Single-Atoms Supported in Crystalline Carbon Nitride as Photocatalysts for Selective C=C Bond Cleavage under Mild Conditions

Izadora R. S. Menezes*1, Gabriel M. de Sousa1, Luis F. G. Noleto1, José B. G. Filho2 and Ivo F. Teixeira1.

Abstract

This work explores isolated Mn single-atoms anchored in poly(heptazine imide) (PHI) for photocatalytic oxidative cleavage of C=C bonds. Mn-PHI materials were synthesized *via* cationic exchange of Na-PHI and characterized by XRD, XAS, EPR, HAADF-STEM, confirming Mn dispersion as single-atoms at low loadings (0.5–1%) and clusters at higher concentrations. Photocatalytic tests revealed Mn-PHI_0.5 achieves 100% conversion of *cis*-stilbene and 100% benzaldehyde selectivity, while higher Mn loadings reduce performance due to cluster and/or nanoparticle formation. The results highlight the superiority of single-atom catalysts for selective C=C bond cleavage under mild conditions.

Keywords: Carbon nitride, Single-atom catalysis and ozonolysis.

Introduction

The oxidative cleavage of C=C bonds is a crucial reaction for synthesizing oxygen-containing functional groups from olefins. While traditional methods like ozonolysis and Lemieux-Johnson oxidation suffer from toxic reagents and safety concerns, molecular oxygen (O2) offers a cleaner, more cost-effective alternative, particularly with transitionmetal complex catalysts (1). However, the inherent limitations of homogeneous catalysis necessitate exploring alternative approaches. Single-atom catalysis (SACs) represents a frontier field that bridges homogeneous and heterogeneous catalysis (2). SACs arise from the ultimate size reduction of metal nanoparticles, where individual metal atoms serve as isolated, stabilized active sites within a support matrix (2,3). These systems combine the welldefined, tunable electronic properties of homogeneous catalysts with the stability, facile separation, and reusability of heterogeneous counterparts, leading to maximized atom efficiency and potentially unique catalytic activities (2-4). Various supports with reactive anchoring functionalities are employed in SACs, including metal oxides, metal-organic frameworks, graphene, and carbon nitrides (4). Building upon the report of polymeric carbon nitrides as metal-free photocatalysts for C=C oxidative cleavage under mild conditions (5) and our group's successful application of transition metals SAs within crystalline carbon nitrides as photocatalysts in diverse oxidation reactions for organic synthesis (6, 7), this study investigates the photocatalytic performance of Mn SAs anchored in poly(heptazine) imide (PHI) for the oxidative cleavage of C=C bonds.

Experimental

Sodium poly(heptazine imide) synthesis

Na-PHI was synthesized using a molten salt approach (8), following the procedure represented in Figure 1. Initially, a 1:10 mass ratio mixture of melamine (C₃H₆N₆, P.A., 99%, Sigma-Aldrich) and sodium chloride (NaCl, P.A., 99%, Neon) was macerated via ball milling for 30 minutes. The resulting mixture was then transferred into an alumina crucible with a lid, which was subjected to thermal treatment in a muffle furnace under an inert nitrogen atmosphere (N2 flow rate: ~80 Lh⁻¹). The temperature was increased at a controlled heating rate of 2.3°Cmin⁻¹ until reaching 600°C, followed by an isothermal hold at this temperature for 4 hours. Upon completion of the thermal treatment and subsequent cooling, the solid product was mixed in deionized water to separate Na-PHI from residual NaCl and soluble by-products. The carbon nitride material was through sequential decantation centrifugation. To ensure the effective removal of unreacted precursors and by-products, the product was subjected to repeated washing with excess water. Finally, the purified Na-PHI was dried in an oven at 80°C for approximately 12 hours.



Figura 1. Na-PHI synthesis scheme.

^{*}menezes.irs@gmail.com

¹Departamento de Ouímica, UFSCar – São Carlos, SP. ²Embrapa Instrumentação - São Carlos, SP.



Metal poly(heptazine imide) preparation by cationic exchange method

The alkali cations into the Na-PHI structure can be easily exchanged by transition metals, leading to a covalent bond between metal and carbon nitride. This feature reveals the ability of PHI structures to anchor metal single-atoms, which was confirmed by a previous publication from our group (9). To prepare Mn-PHI (Figure 2), 10 mL of an aqueous solution of manganese chloride tetrahydrate (MnCl₂·4H₂O, P.A., 98%, Êxodo) was prepared at a predetermined concentration (Table 1), corresponding to the desired metal loading in the final PHI material. Subsequently, 500 mg of Na-PHI was dispersed in the solution under vigorous shaking, followed by sonication for 30 minutes. The resulting mixture was centrifuged to isolate the solid product, which was then washed repeatedly (3 times) with deionized water to remove residual salts. After centrifugation, the purified material was dried in an oven at 80°C for approximately 12 hours. The synthesized materials were named based on the incorporated metal and its target concentration, i.e. Mn-PHI prepared to reach 0.5% of Mn in the matrix was named as Mn-PHI 0.5.



Figure 2. Mn-PHI preparation scheme.

Characterization

Flame Atomic Absorption Spectroscopy (FAAS)

To determine the actual metal content in the photocatalysts prepared, firstly, the M-PHI samples were opened by adding 2 mL of a 1:1 concentrated sulfuric acid (H₂SO₄, P.A. 98%, Qhemis) aqueous solution to 20 mg of the sample and digesting it at approximately 130°C for 1h. Then, the resulting mixture was diluted to 15 mL with deionized water and analysed using a Flame Atomic Absorption Spectrometer (model: Varian AA240FS). The measurements were performed at Laboratório de Espectrometria de Absorção Atômica (LEAA) - NEPS-DQ, UFMG.

X-Ray Diffraction (XRD)

Powder XRD (P-XRD) patterns were measured using equipment from Bruker (model D8 Advance Eco), with radiation Cu-K α_1 (1.54 Å) operating with 1 kW power (25 mA x 40 kV). The diffractograms were obtained in the range of 5-50°, with a scanning time of 15 min and a step of 0.02°. The experiments were conducted at the Laboratório de Caracterização Estrutural (LCE) – DEMa, UFSCar.



Electron Paramagnetic Resonance Spectroscopy (EPR)

EPR measurements of Mn-PHI were conducted using a Bruker EMX Plus spectrometer (X-band, ~9.8 GHz). Each sample was loaded into a standard quartz EPR tube, inserted into the cavity, and measured. The spectra were normalized by the mass of the solid sample. Experiments were performed at Instituto de Química de São Carlos (IQSC) - USP.

High-Angle Annular Dark-Field Scanning Transmission Electron Microscopy (HAADF-STEM)

For scanning transmission electron microscopy (STEM) analysis, the catalyst was dispersed in 2-propanol via ultrasonication (10 min) and drop-casted onto a Cu holey carbon TEM grid. Imaging was performed using a Thermo Fisher Scientific Titan Cubed Themis (TEM-Titan) microscope operated at 300 kV, equipped with a cold-field emission gun (FEG) and double Cs aberration correction. HAADF-STEM images were acquired with a probe convergence semi-angle of 25 mrad. To minimize hydrocarbon contamination during high-magnification imaging, a 30-minute "beam shower" pretreatment was applied. All experiments were conducted at the Laboratório Nacional de Nanotecnologia (LNNano) - CNPEM.

X-ray Absorption Spectroscopy (XAS)

XAS measurements were conducted at Beamline 6-BM (BMM, Beamline for Materials Measurements) of the National Synchrotron Light Source II (NSLS-II) at Brookhaven National Laboratory - New York, USA. The broadband X-ray beam was generated using a 3-pole wiggler source, covering an energy range of 4.0–23.0 keV with a spot size of 300 μm . A Si(111) monochromator provided an energy resolution of $1.2\times10^{-4}\,\Delta E/E$ and a flux of 2×10^{12} photons/s at 10.0 keV. For energy calibration and spectral alignment during data analysis, a Mn metal foil reference was measured simultaneously with all XAS spectra. Data processing and fitting of Extended X-ray Absorption Fine Structure (EXAFS) spectra were performed using ATHENA software package.

Photocatalysis tests

The photocatalytic activity of Mn-PHI for the oxidative cleavage of the double bond was tested in a 4 mL septum cap vials, adding 25 mg of the material, 2 mL of acetonitrile (CH₃CN, 99%, gradient grade for HPLC, Merck) as solvent and 7 μL (40 μmol) of *cis*-stilbeno (C₁₄H₁₂, 96%, P.A., Sigma-Aldrich) as substrate. A magnetic bar was added for stirring and, after sealing, O₂ was bubbled to the reaction mixture for 1 min. The vials were placed in the cube reactor, which contains a 410 nm LED (10 W) as an irradiation source at the bottom of the vials holes and is connected to a circulator bath for temperature control. The reaction was conducted at 25°C for 24h. Then, the liquid was separated from the photocatalyst by centrifugation (14000 RPM for 15 min) and diluted 2 times in acetonitrile for analysis in Gas



Chromatography coupled with Mass Spectrometry (GM-MS). The peaks in the chromatogram were identified and integrated for the calculation of conversion and selectivity.

Results and Discussion

Photocatalyst characterization

As discussed in a previous work of our group, to conduct the cationic exchange of Na⁺ to Mn²⁺ ions in the PHI matrix is necessary to expose the matrix to an excess of transition metals. We suggested an initial metal concentration to reach a desired metal content in the final M-PHI (9). To assess if Mn-PHI follows the same recommendation, the Mn concentrations in the materials prepared were determined, and the results are presented in Table 1. As shown, the introduction of 0.5 to 4% of Mn into PHI sticks to the method, but at a higher tentative concentration of 10% there is a saturation of Mn-PHI in the structure. This indicates that the metal coordination and/or interaction sites in the matrix might be limited.

Table 1. Solution concentration for Mn-PHI preparation, and theoretical *vs* measured Mn concentrations in the prepared PHI materials

materials.			
	MnCl ₂ .4H ₂ O solution (molL ⁻¹)	Theoretical Mn (%m/m)	Measured Mn (%m/m)
Na-PHI	-	-	0.006
Mn-PHI_0.5	0.005	2.0	0.4
Mn-PHI_1	0.01	3.9	0.9
Mn-PHI_2	0.02	7.9	2.0
Mn-PHI_4	0.04	15.6	4.3
Mn-PHI_10	0.1	39.1	5.5

In addition to quantifying metal content, determining Mn's structural form, whether as single-atoms, clusters and/or nanoparticles, is crucial. While XRD primarily characterizes the PHI crystalline structure (indexed in a hexagonal lattice, space group P31m) (10), it can also reveal potential Mn agglomeration through detection of crystalline Mn phases. Figure 3 presents the XRD patterns of synthesized materials, showing characteristic peaks at 8.3°, 14.3°, 21.8°, 36.3° and 44.1° (attributed to in-plane periodicity of heptazine units) and a broad feature between 22°-30° (corresponding to the stacked layered structure of Na-PHI) (9,10). The Mn-PHI patterns exhibit subtle but distinct differences in peak intensities and shapes compared to Na-PHI, suggesting lattice distortions from metal exchange. These modifications may also reflect increased turbostratic disorder, particularly at higher metal loadings, where larger metal volumes incorporated between heptazine layers disrupt structural ordering. The acidic nature of the MnCl₂·4H₂O precursor solution may further contribute to crystallinity reduction during Mn-PHI preparation. Critically, no diffraction signals corresponding to crystalline



Mn compounds (e.g., oxides or chlorides) were detected, strongly indicating Mn exists as highly dispersed species within the matrix. The standard diffraction pattern of MnO is presented in the figure as an example of lack of manganese oxide peaks in the Mn-PHI materials (other compounds were also checked, such as MnO₂).

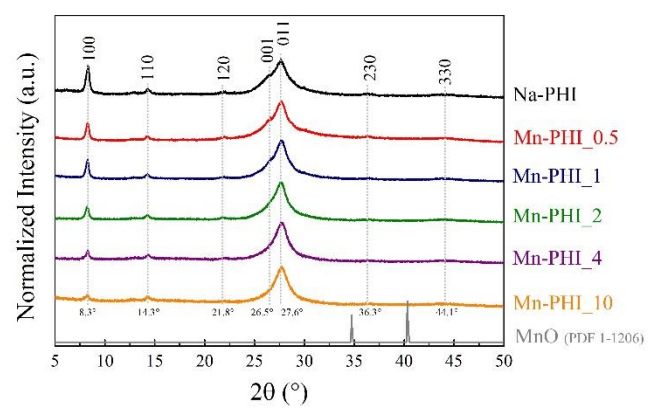


Figure 3. XRD patterns for M-PHI.

Apart from some limitations, EPR spectra can also give information on the dispersibility state of Mn in the PHI structure (11). We measured some of the prepared samples, and the results are shown in Figure 4. In the intensitynormalized spectra, a signal with a g-factor of approximately 2.00 is observed (8). This signal broadens as the manganese content increases within the Na-PHI polymeric matrix. This signal is attributed to Mn²⁺. At Mn-PHI 0.5 and 1, transitions arising from the hyperfine coupling between the 55 Mn nuclei (I = 5/2) and the unpaired electrons are evident. This interaction results in the appearance of six hyperfine transition lines (derived from the 2I+1 rule), which are characteristic of isolated Mn²⁺ species within the semiconductor structure. Conversely, if the interaction between electron spins becomes sufficiently strong due to shorter distances between paramagnetic centers, the hyperfine structure of the spectrum collapses, resulting in signal broadening, as is the case for Mn-PHI_2 (11,12). It should be noted that while clusters might be present in Mn-PHI 0.5 and 1, a substantial portion of the incorporated Mn²⁺ remains highly dispersed throughout the material. Meanwhile is evident that on Mn-PHI 2 the clusters are more present.



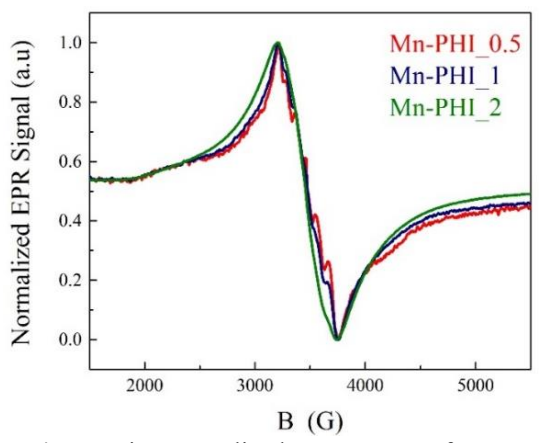


Figure 4. Intensity-normalized EPR spectra of Mn-PHI.

Since HAADF-STEM can provide direct real-space visualization of individual heavy atoms supported on a lighter substrate like carbon nitride, it is considered one of the main methods to identify single-atoms (11). However, it is an advanced technique with limited accessibility. Initially, we obtained TEM images of Mn-PHI 0.5 and Mn-PHI 2, which are presented in Figures 5 and 6. The images in low magnification of Mn-PHI 2 showed in Figure 6 a-c, indicate that the material consists of large, flat, stacked, µm-sized flakes. The fringes related to the ordered structure of PHI is also noted in Figure 6f, confirming the matrix's crystalline nature. The Mn EDS mapping (Figure 6 d and e) disclose small spots and larger bright areas, indicating the presence of isolated dispersed Mn and clusters/nanoparticles. The high magnification image (scale 5 nm) of Mn-PHI 2 (Figure 5b) revealed the crystalline structure of the MnO nanoparticles. Images of Mn-PHI 0.5 showed considerably less nanoparticles present in the matrix, and the high magnification image (scale 2 nm) in Figure 5a it is clear the presence of isolated Mn atoms in the PHI support.

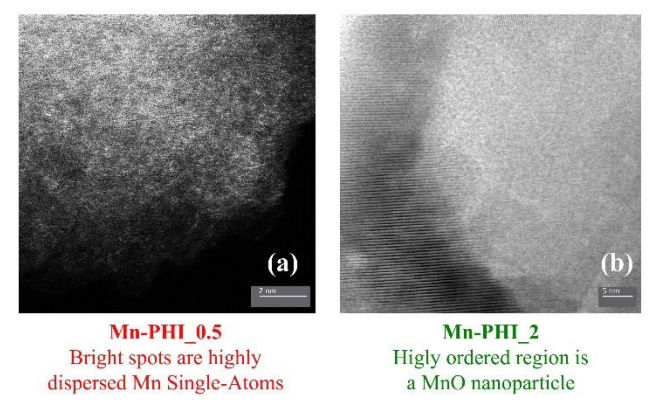


Figure 5. HAADF-STEM images in high magnification of **(a)** Mn-PHI_0.5 where brighter spots represent Mn isolated single-atoms and **(b)** Mn-PHI_2 where highly ordered region in the left is related to a MnO nanoparticle.



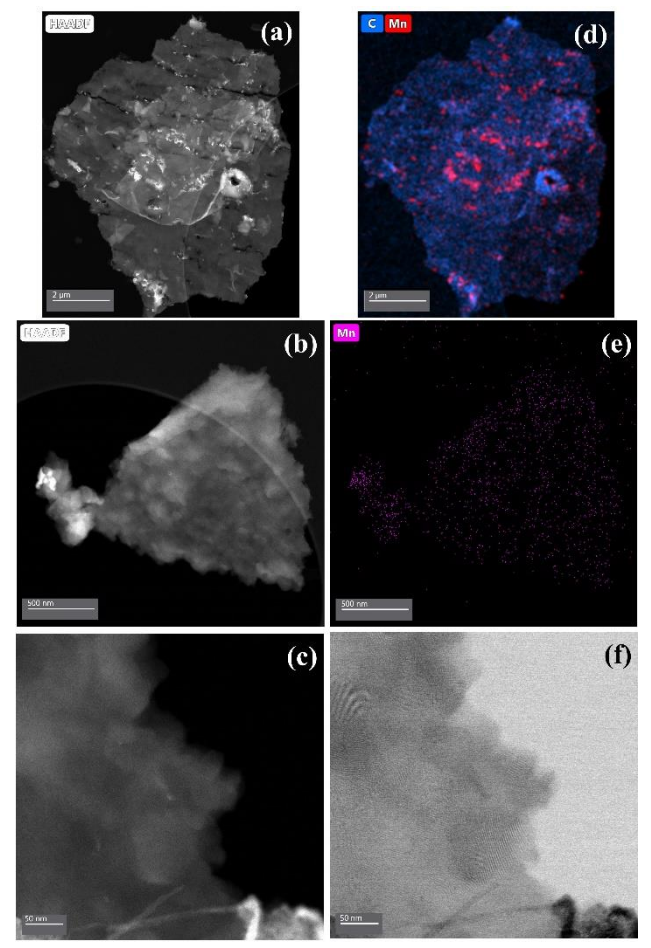


Figure 6. (a), **(b)** and **(c)** HAADF-STEM images where brighter areas represent Mn; **(d)** and **(e)** BF-STEM images with Mn EDS mapping of (a) and (b) regions, respectively; **(f)** BF-STEM image of (c) region showing fringes of PHI crystalline characteristic structure. All images are from Mn-PHI 2 sample and in low magnification.

XAS is another advanced method considered gold standard for identification of single-atoms. It is elementspecific and provides information about the electronic and local atomic structure around the metal center. It's highly sensitive to the oxidation state, coordination number, and the type and distance of neighbouring atoms. The Extended X-ray Absorption Fine Structure (EXAFS) can confirm the absence of metal-metal bonds and reveal the coordination environment (e.g., M-N bonds) (13). The radial distance distributions obtained after treatment of the EXAFS region of XAS spectra of Mn-PHIs are presented in Figure 7. For all materials prepared and for manganese oxide (MnO) reference, it is noted a peak around 1.7 Å associated with Mn-N or Mn-O bonds. This confirms that Mn is coordinated into the PHI structure. The peak around 2.7 Å related to Mn-Mn bonds in the second shell of atomic interaction is observed only for MnO reference. This is strong evidence of



isolated Mn atoms in the Mn-PHI materials, confirming the presence of single-atoms for all materials and no presence of metal agglomerates. However, this contradicts the results given by EPR and HAADF-STEM analysis for the Mn-PHI_2 sample, where it was observed the material has clusters and nanoparticles. This discrepancy might be explained by EXAFS limitation on detecting clusters that are less than 10% of total Mn content or are highly disordered (14).

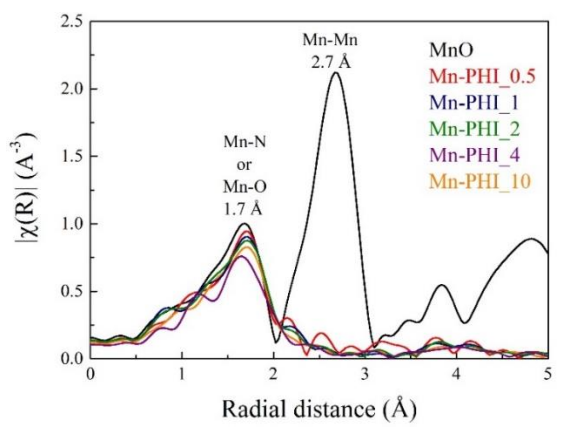


Figure 7. Fourier transformed (FT) EXAFS spectrum (R-space).

In conclusion, all Mn-PHI samples have isolated Mn single-atoms and clusters/nanoparticles supported in the matrix. However, as lower the metal loading, lower is the aggregation of Mn in the structure, leading to more predominant Mn single-atoms sites. Meanwhile, in higher concentrations of Mn in the PHI (e.g. Mn-PHI_2) agglomeration seems to occur, leading to more formation of clusters and nanoparticles sites.

Photocatalysis tests

The results concerning the conversion of cis-stilbeno and selectivity towards the production of benzaldehyde using Mn-PHI materials as photocatalysts for the oxidative cleavage reaction are presented in Figure 8. Interestingly, the lowest Mn loading in the crystalline carbon nitride gave 100% conversion of cis-stilbeno, with 100% selectivity for benzaldehyde. Increasing Mn concentration in the photocatalyst, reduces the conversion of the substrate and leads to the production of by-products (stilbene oxide and phenylacetaldehyde). This indicates the better performance of single-atoms catalysis for this type of reaction in comparison to clusters/nanoparticle catalysis. optimization of the photocatalytic reaction should be further explored, varying catalyst quantity, substrate concentration, reaction time, temperature, solvents, oxidants and additives. The reproducibility of the reaction, scope tests, and reuse of the catalyst alongside mechanistic and kinetic investigations are also going to be studied.



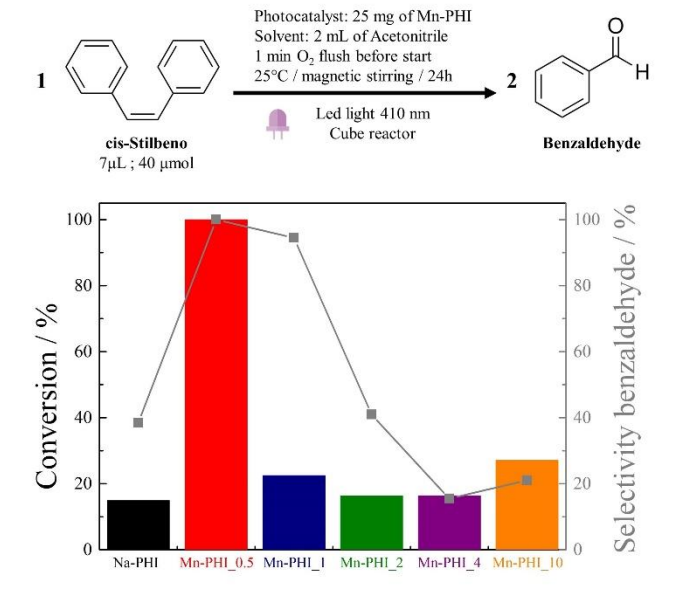


Figure 8. Conversion and selectivity results of photocatalytic tests.

Conclusions

This study successfully anchored single-atom Mn into the PHI structure by the cation exchange method, creating an efficient photocatalyst for the oxidative cleavage of C=C bonds. Characterization techniques (XAS, EPR, HAADF-STEM) pointed that low Mn loadings (0.5–1%) resulted in mainly highly dispersed single atoms, while higher concentrations ($\geq 2\%$) led to more cluster formation. Photocatalytic tests demonstrated that Mn-PHI 0.5 achieved complete conversion of cis-stilbene with full selectivity for benzaldehyde, whereas materials with higher Mn content showed diminished performance due to metal agglomeration-induced side reactions. These findings underscore the critical role of single-atom dispersion in maximizing catalytic efficiency and selectivity. Furthermore, this work demonstrates a milder alternative for typical ozonolysis reactions, paying the way for sustainable. metal single-atoms based photocatalysts in organic synthesis.





Acknowledgements

The authors are deeply grateful to the following facilities for experimental analysis: DQ-UFSCar, DEMa-UFSCar, NEPS/DQ-UFMG, IQSC – USP, Embrapa Instrumentação, LNNano – CNPEM and NSLS-II-Brookhaven National Laboratory.

This work was funded by FAPESP, CNPq, CAPES and FINEP.

Artificial intelligence (AI) tools were used to check grammar, spelling, and improve readability and language. It was also used to write the abstract and conclusion sections, which were human-edited.

References

- Z. Huang; R. Guan; M. Shanmugam; E. L. Bennett; C. M. Robertson; A. Brookfield; E. J. L. McInnes; J. Xiao. *J. Am. Chem. Soc.* 2021, *143* (26), 10005-10013.
- S. F. Yuk; G. Collinge; M. T. Nguyen; M.S. Lee; V. A. Glezakou; R. Rousseau in Advanced Heterogeneous Catalysts Volume 2: Applications at the Single-Atom Scale, P. Sudarsanam and L. Singh, Ed.; American Chemical Society, 2020; Chapter 1, 1-15.
- 3. W. Zhang; Q. Fu; Q. Luo; L. Sheng; J. Yang. *JACS Au* **2021** *1* (12), 2130-2145.
- 4. V. B. Saptal; V. Ruta; M. A. Bajada; G. Vilé. *Angew. Chem. Int. Ed.* **2023**, *62* (*34*), e202219306.
- Y. Zhang; N. Hatami; N. K. Lange; E. Ronge; W. Schilling; C. Jooss; S. Das. *Green Chem.* 2020, 22, 4516-4522.
- M. A. R. Silva; N. V. Tarakina; J. B. G. Filho, C. S. Cunha; G. F. S. R. Rocha; G. A. A. Diab; R. A. Ando; O. Savateev; I. Agirrezabal-Telleria; I. F. Silva; S. Stolfi; P. Ghigna; M. Fagnoni; D. Ravelli; P. Torelli; L. Braglia; I. F. Teixeira. *Adv. Mater.* 2023, 35, 2304152(1-13).
- W. L. Oliveira; M. A. R. Silva; G. A. A. Diab; J. B. G. Filho; V. G. S. Pastana; L. L. B. Silva; E. F. Oliveira; W. V. F. C. Batista; T. S. Cruz; V. R. Mastelaro; M. J. M. Pires; I. F. Teixeira; J. P. Mesquita. ChemPhotoChem 2025, 9, e202400130.
- 8. Z. Chen; A. Savateev; S. Pronkin; V. Papaefthimiou; C. Wolff; M. G. Willinger; E. Willinger; D. Neher; M. Antonietti; D. Dontsova. *Adv. Mater.* **2017**, *29*, 1700555.
- F. M. Colombari; M. A. R. Silva; M. S. Homsi; B. R. L. Souza; M. Araujo; J. L. Francisco; G. T. S. T. Silva; I. F. Silva; A. F. Moura; I. F. Teixeira. *Faraday Discuss.*, 2021, 227, 306-320.
- M. A. R. Silva; I. F. Silva; Q. Xue; B. T. W. Lo; N. V. Tarakina; B. N. Nunes; P. Adler; S. K. Sahoo; D. W. Bahnemann; N. L. Salas; A. Savateev; C. Ribeiro; T. D. Kühne; M. Antonietti; I. F. Teixeira. *Applied Catalysis B: Environmental*, 2022, 304, 120965.
- 11. M. Agrachev; V. Giulimondi; I. Surin; S. Mitchell; G. Jeschke; J. Pérez-Ramírez. *Chem Catalysis* **2024**, *4* (12), 101136.
- P. K. Sahoo; R. Maiti; P. Ren; J. J. D. Jaén; X. Dai; G. Barcaro; S. Monti; A. Skorynina; A. Rokicińska; A. Jaworski; L. Simonelli; P. Kuśtrowski; J. Rabeah; S. Das. J.Am. Chem. Soc. 2025, 147, 11829–11840.
- 13. Z. Chen; A. G. Walsh; P. Zhang; *Acc. Chem. Res.* **2024**, *57 (4)*, 521-532.
- 14. J. Finzel; K. M. S. Gutierrez; A. S. Hoffman; J. Resasco; P. Christopher; S. R. Bare. *ACS Catal.* **2023**, *13* (*9*), 6462–6473.